UC Irvine
UC Irvine Previously Published Works

Title

Confinement degradation by Alfvén-eigenmode induced fast-ion transport in steady-state scenario discharges

Permalink

https://escholarship.org/uc/item/95k514bd

Journal

Plasma Physics and Controlled Fusion, 56(9)

ISSN

0741-3335

Authors

Heidbrink, WW
Ferron, JR
Holcomb, CT
et al.

Publication Date

2014-09-01

DOI

10.1088/0741-3335/56/9/095030

Copyright Information

Peer reviewed

Confinement degradation by Alfvén-eigenmode induced fast-ion transport in steady-state scenario discharges

W W Heidbrink[1], J R Ferron[2], C T Holcomb[3], M A Van Zeeland[2], Xi Chen[4], C M Collins[1], A Garofalo[2], X Gong[5], B A Grierson[6], M Podestà[6], L Stagner[1] and Y Zhu[1]

[1] University of California Irvine, Irvine, CA, USA
[2] General Atomics, San Diego, CA, USA
[3] Lawrence Livermore National Laboratory, Livermore, CA, USA
[4] Oak Ridge Institute for Science Education, Oak Ridge, TN, USA
[5] Institute of Plasma Physics, Chinese Academy of Sciences, Hefei, People's Republic of China
[6] Princeton Plasma Physics Laboratory, Princeton, NJ, USA

E-mail: Bill.Heidbrink@uci.edu

Abstract
Analysis of neutron and fast-ion D_α data from the DIII-D tokamak shows that Alfvén eigenmode activity degrades fast-ion confinement in many high β_N, high q_{min}, steady-state scenario discharges. (β_N is the normalized plasma pressure and q_{min} is the minimum value of the plasma safety factor.) Fast-ion diagnostics that are sensitive to the co-passing population exhibit the largest reduction relative to classical predictions. The increased fast-ion transport in discharges with strong AE activity accounts for the previously observed reduction in global confinement with increasing q_{min}; however, not all high q_{min} discharges show appreciable degradation. Two relatively simple empirical quantities provide convenient monitors of these effects: (1) an 'AE amplitude' signal based on interferometer measurements and (2) the ratio of the neutron rate to a zero-dimensional classical prediction.

Keywords: tokamaks, fast particle effects, Alfvén waves, fusion product effects

(Some figures may appear in colour only in the online journal)

1. Introduction

Steady-state operation at high plasma pressure may improve the attractiveness of tokamak plasmas for fusion energy production [1]. In order to maintain the plasma in steady-state, the plasma current must be driven fully noninductively. Since the fraction of the total current carried by the intrinsic bootstrap current increases with the safety factor and normalized plasma pressure as $f_{BS} \propto q\beta_N$, [2, 3] operation at high β_N minimizes the power required for externally driven current. Values of β_N between 2.5–3.5 and edge safety factor $q_{95} \sim 5$ are envisioned for the steady-state ITER operating scenario [2].

Demonstration of a high β_N, steady-state operating scenario has been a major goal of the DIII-D program for decades [4]. In recent years, to achieve steady-state 'high q_{min}' scenarios with broad current and pressure profiles, the facility has added additional gyrotron power for off-axis electron cyclotron current drive (ECCD) and tilted a beam line to inject off-axis. Recent publications have noted a tendency for reduced confinement with increasing q_{min} [5–8]. For example, figure 6 of [8] shows the scaling of the energy confinement time with q_{min} for a database of steady-state scenario discharges. When normalized to a standard ('H89') global energy-confinement scaling law [9], the discharges

with $q_{min} \gtrsim 2$ have global (i.e. thermal plus fast-ion) confinement below typical H-mode levels; nevertheless, the thermal confinement time is consistent with typical ('H98') H-mode values. Other publications [6, 7] state that the observed dependency of thermal transport on the q profile deviates from gyrokinetic predictions. These observations motivate the present study.

This paper investigates two hypotheses: (1) 'Are Alfvén eigenmodes (AEs) responsible for degraded fast-ion confinement in high q_{min} discharges?' and (2) 'Can fast-ion transport account for degraded global confinement?' The answer to both questions is 'yes.'

It is well known that AEs can cause appreciable fast-ion transport [10–12]. In DIII-D, for diagnostic reasons, the vast majority of AE studies have been in low-density, L-mode plasmas during the current ramp; see the introduction of [13] for a summary of results in current-ramp plasmas. In steady-state scenario plasmas, there have been previous indications of a connection between Alfvénic activity and fast-ion behavior on both DIII-D [14–16] and on other devices [17, 18]. This paper presents the first systematic examination of fast-ion transport by AEs in steady-state scenario DIII-D plasmas.

Theoretically, there are three reasons that high q_{min} scenarios could be more susceptible to AE activity. First, elevated scenarios allow fast ions to drive and interact with AE instabilities more effectively through higher order resonances [19]. These higher order resonances are particularly important in DIII-D plasmas, since the 80 keV beam energies are not able to fulfill the fundamental $v_{\parallel} = v_A$ resonance at normal toroidal fields. (Here, $v_{\parallel}$ is the fast ion parallel velocity and v_A is the Alfvén speed.) Second, scenarios with elevated q_{min} often have weak or reversed magnetic shear, and these types of q profiles result in wider modes with weaker continuum interaction that can resonate with the energetic particle population over a larger radial range. Third, the larger banana width in a weak poloidal field increases edge charge-exchange losses and allows fast-ion loss boundaries to penetrate further into the core of the plasma.

This article begins by describing the experimental conditions, diagnostics, and analysis techniques (section 2). The correlation between AEs and degraded fast-ion confinement appears next (section 3). Section 4 shows that the reduction in fast-ion power to the thermal plasma can explain the global confinement degradation, without any need for enhanced thermal transport. The final section explains why simple empirical measures of AE activity and fast-ion confinement provide excellent diagnostics of plasma behavior in these discharges. A conclusion and outlook are also given.

2. Experiment

With one exception, the discharges in this study use plasma shapes and plasma initiation techniques that are similar to those described in [5, 20]. Figure 1 shows a pair of extensively analyzed discharges. The evolution of the plasma current, density, beam power, timing of the H-mode transition, normalized beta, application of ECCD power, and active correction of $n = 1$ static fields are all important factors

in achieving a steady-state, high β_N condition with minimal tearing-mode activity. For the purpose of this study, discharges that achieve quasi-stationary conditions for $\gtrsim 0.5$ s are useful shots, even if the non-inductive current fraction differs from unity.

Up to six co-injected deuterium neutral-beam sources are employed. Generally, a mixture of near-tangential (tangency radius $R_{tan} = 1.15$ m) and near-perpendicular ($R_{tan} = 0.76$ m) sources as well as off-axis and on-axis sources inject (figure 2(a)). The pitch of the magnetic field line is chosen to maximize neutral-beam current drive (NBCD) from the off-axis beams [21]. The beam injection energy is usually 81 keV, although a few discharges with lower voltages of ~65 keV are included in the study. For diagnostic purposes, a single counter-injected source injects infrequent 10 ms pulses but this source injects less than 3% of the average beam power. When employed, the gyrotrons for ECCD deposit power in a broad range near the half-radius.

All but one of the discharges have the elongated, double-null divertor shape shown in figure 2(b). The toroidal field varies from $B_T = 1.0$–2.1 T.

For comparison purposes, one discharge from a different set of experiments is included. In collaboration with scientists from the Chinese Academy of Sciences, those experiments strove to develop a high β_N, steady-state scenario for the Experimental Advanced Superconducting Tokamak (EAST). A detailed description of that experiment will appear elsewhere. The shape for the EAST-demonstration discharge is also a double-null divertor with elongation $\kappa \simeq 1.8$ but the triangularity is different than the other plasmas. The neutral beam and ECCD sources are used similarly, however.

Figure 3 shows plasma profiles for three different discharges in the study. Thomson scattering [22] and four interferometers [23] measure the electron density n_e, Thomson scattering and an electron cyclotron emission (ECE) radiometer (for $B_T \geqslant 1.7$ T) measure the electron temperature T_e, charge-exchange recombination (CER) spectroscopy of carbon [24] measures the ion temperature T_i and toroidal rotation f_{rot}, Z_{eff} is inferred from the CER measurement assuming that carbon is the dominant impurity, and the q profile is obtained from EFIT [25] reconstructions that utilize magnetics and motional Stark effect (MSE) [26] data. The error bars show the temporal variance in the fitted profiles over the analyzed quasi-stationary portion of the discharge; this should accurately represent random errors but neglects any systematic errors in the diagnostic data or fitting procedure. Comparing the discharges, all three discharges have an H-mode pedestal at the edge. The EAST-demonstration discharge has an internal transport barrier (most obvious in the T_e profile), higher overall density, and very high q_{min}.

Virtually every discharge has AE activity and many also have unstable tearing modes. Figure 4 shows spectra calculated from the cross-power of two CO_2 interferometer signals [27] for the $q_{min} \gtrsim 2$ and $q_{min} \gtrsim 1$ discharges shown in figures 1 and 3. The $q_{min} \gtrsim 1$ shot has a tearing mode with frequency ~20 kHz throughout the time of interest (figure 4(a)); the $q_{min} \gtrsim 2$ shot also has a persistent tearing mode at ~29 kHz (not shown). The toroidal mode numbers of these tearing
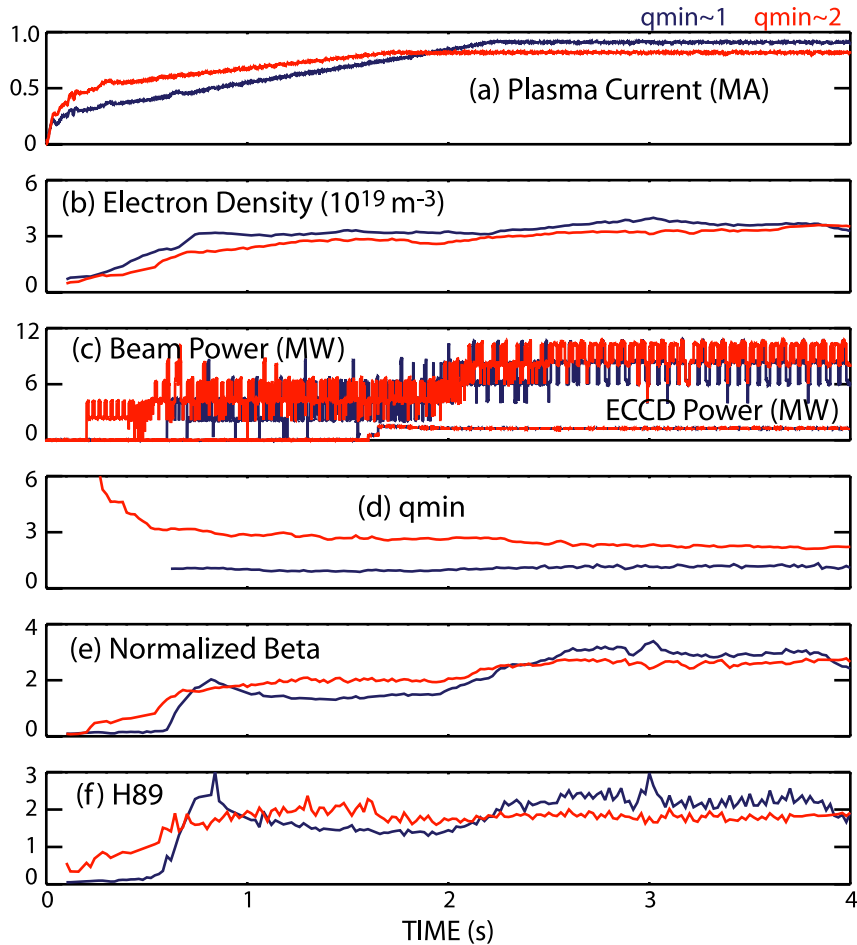
Figure 1. (*a*) Plasma current I_p, (*b*) line-average electron density $\bar{n}_e$, (*c*) injected beam (solid) and ECCD (dashed) power, (*d*) q_{min}, (*e*) β_N, and (*f*) normalized confinement time H_{L89} versus time in a matched pair of discharges with $q_{min} \gtrsim 1$ (#153071) and $q_{min} \gtrsim 2$ (#153072). $B_T = 1.8$ T.
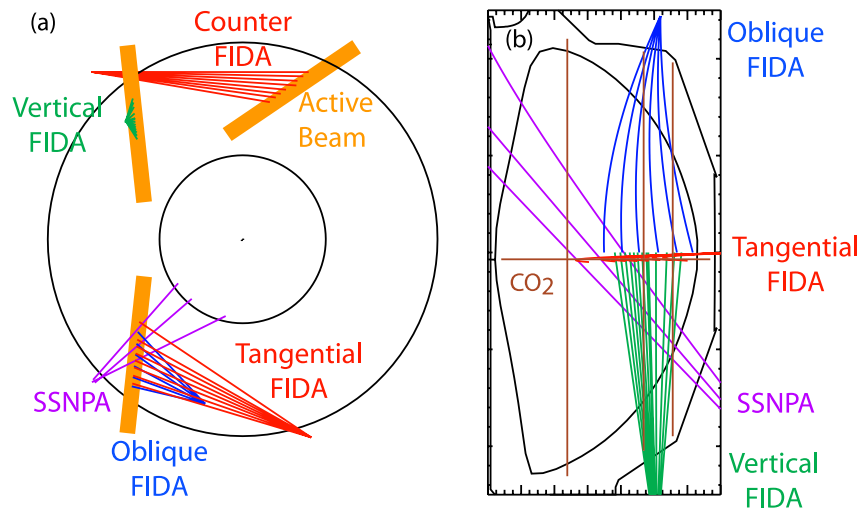
Figure 2. (*a*) Plan and (*b*) elevation views of DIII-D. The three active beams for fast-ion diagnostics are indicated by thick lines and the view chords of the SSNPA and vertical, oblique, tangential, and counter-viewing FIDA sightlines are shown. The elevation also shows the positions of the four interferometer chords and the last-closed flux surface for the majority of plasmas in this study.

modes, as inferred from a toroidal array of Mirnov coils [28], is $n = 2$. In the plasma frame, the nominal frequency of toroidal Alfvén eigenmodes (TAE) $f_{TAE} = v_A/(4\pi qR)$ is approximately 94 and 67 kHz in these two discharges. A

large number of modes are observed above the nominal TAE frequency, especially in the $q_{min} \gtrsim 2$ discharge. Reliable measurements of the toroidal mode numbers of the modes above f_{TAE} are unavailable in this pair of discharges but, in
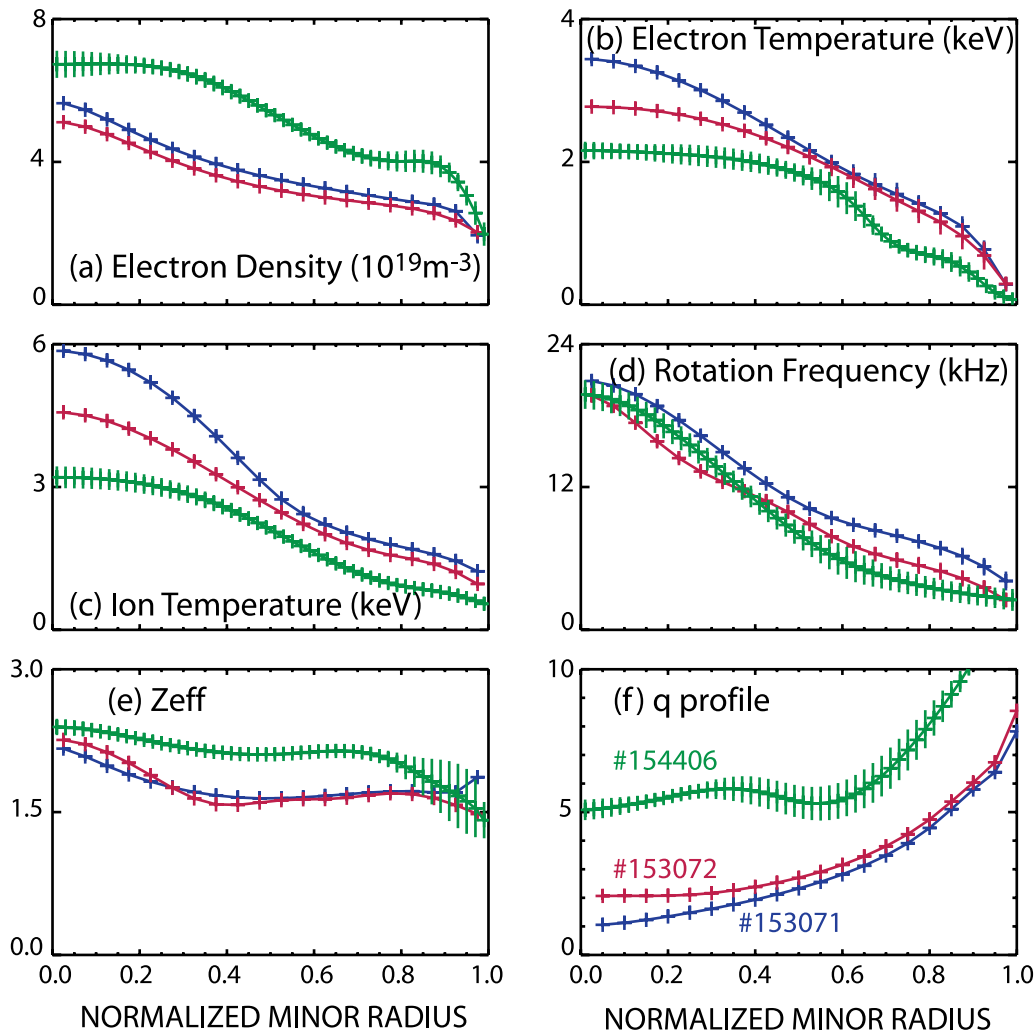
Figure 3. Profiles of (*a*) n_e, (*b*) T_e, (*c*) T_i, (*d*) toroidal rotation frequency, (*e*) Z_{eff}, and q versus ρ for the matched pair of discharges between 3.2–3.7 s (section 3.1) and the outlier discharge between 5.4–5.8 s (section 3.3). The classically predicted fast-ion stored energy is 36%, 28% and 17% of the total for discharges #153072, #153071, and #154406, respectively.

other discharges with similar spectra, the modes have $n = 2$–7. These are typical values for DIII-D and follow the generally observed scaling [12] that modes with $k_r \rho_f \sim 1$ are most unstable. (Here k_r is the AE radial wavenumber and ρ_f is the fast-ion gyroradius.) Including the Doppler shift $n f_{rot}$, the observed modes have typical TAE frequencies. Where available, radial profiles from the ECE and beam emission spectroscopy (BES) [29] diagnostics show that some of the observed modes in this study are core-localized, some have maximum amplitudes near mid-radius, and some peak near the edge.

Although it is relatively easy to classify the virulence of Alfvén activity qualitatively, finding a quantitative algorithm that agrees with qualitative classification is challenging. A recent study [13] successfully used ECE data for a quantitative measure of AE amplitude but, in the present work, ECE data are unavailable at high density and low toroidal field, so an alternative diagnostic is needed. Here, we use the data from four interferometer chords (figure 2) to develop a quantitative measure of AE activity. First, the cross-power and coherence of all six combinations of interferometers is computed. A valid

mode satisfies the following criteria.

- The signal must be 30% larger than the background and the coherency must be above 85%.
- The frequency must be greater than the smaller of the estimated TAE frequency and geodesic acoustic mode (GAM) frequency. (A typical value for the GAM frequency is 60 kHz.)
- The frequency is below 250 kHz.
- The time slice does not coincide with an edge localized mode (ELM).
- A valid peak appears on at least four of the six interferometer pairs.

Once the valid peaks are identified, the cross-power is summed for each time slice and divided by the line-average densities. The median normalized cross-power is calculated for the entire quasi-stationary window. The 'AE amplitude' is the square root of the normalized, summed, median cross-power. For the spectra in figure 4(*b*), the 'AE amplitude' is 3.5 while, for the spectra in figure 4(*a*), the 'AE amplitude' is 1.0. This is consistent with the qualitative assessment that the $q_{min} \gtrsim 2$
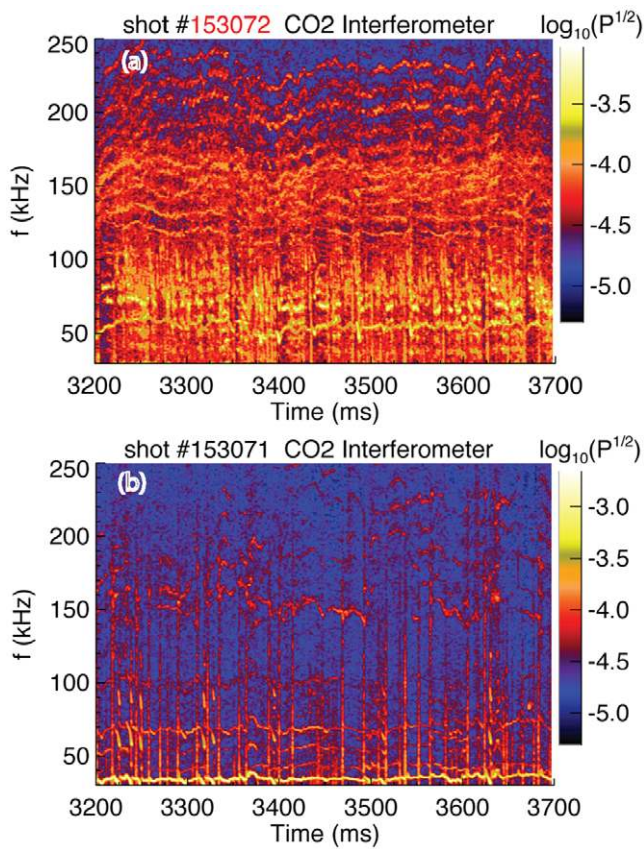
Figure 4. Cross-power of the two most central interferometer channels in (*a*) the $q_{min} \gtrsim 1$ discharge and in (*b*) the $q_{min} \gtrsim 2$ discharge.

case has strong AE activity, while the $q_{min} \gtrsim 1$ case has weak but nonzero AE activity.

An extensive set of instruments diagnose the confined fast ions. The volume-averaged neutron rate is measured by a ZnS scintillator that is cross-calibrated to fission counters [30]. The fast-ion pressure is inferred from the difference between the equilibrium pressure and the measured thermal pressure; when integrated over the volume, this also provides a measurement of the stored fast-ion energy W_f.

Spectroscopic fast-ion D_α (FIDA) measurements are available for four different nominal viewing angles (figure 2): vertical, oblique, tangential, and counter. Each system uses a different set of spectrometers and CCD cameras. A 12-channel profile from a nominally vertical view is obtained by a pair of CER spectrometers that are tuned to the blue-shifted side of the cold D_α line and acquire data in 2.5 ms time bins with a transverse spatial resolution of $\lesssim 1$ cm. The oblique, six-channel profile with a viewing angle of $\sim 45°$ comes from bandpass-filtered blue-shifted spectra acquired in 1 ms time bins with a transverse spatial resolution of ~ 5 cm [31]; this system has the best signal-to-noise but poorest spatial resolution. The tangential views of co-going and counter-going fast ions come from the 'main-ion CER' system [32]. To avoid the bright beam emission from the active beam, the co-going tangential system views a counter-injected heating beam and measures the blue-shifted spectrum, while the counter-going tangential system views a co-injected heating beam and

measures the red-shifted spectrum. Both tangential systems acquire data in 5 ms time bins.

Obtaining valid FIDA data is a diagnostic challenge. The DIII-D FIDA diagnostics rely upon three different active beams for their signals (figure 2(*a*)). The FIDA signal is obtained from the difference between spectra acquired when the active beam is on and when the beam is off (figure 5). Unfortunately, all of the sightlines also observe light produced by neighboring neutral-beam sources. To avoid contamination, these neighboring sources must remain in a constant state during the on/off comparison. In normal steady-state scenario operation, the beam power is modulated to feed back on a selected value of β_N. Since power from a majority of sources is needed to obtain high β_N, complicated beam programming is required to meet simultaneously the diagnostic and scenario requirements. Another complication is the prevalence of ELMs during H-mode operation, since ELMs can cause rapid changes in background light. For the data presented here, most time slices have been discarded due to ELM contamination and all retained time slices have been individually examined to insure stationary backgrounds; without the many time bins provided by quasi-stationary operation, valid spectra would be unavailable. Because the neutron rate is appreciable, spikes on one or two pixels frequently appear in the spectra but these are readily removed by interpolation. The final step in analysis of the FIDA spectra is to integrate the net signal over a range of wavelengths. The selected wavelengths correspond to energies along the line-of-sight of 25–68 keV.

Active charge-exchange measurements are available for three different radial sightlines (figure 2). A solid-state neutral particle analyzer (SSNPA) operated in current mode [33] is employed for these measurements. As with the FIDA measurements, careful timeslice selection is employed to avoid contamination by neighboring beams or ELMs.

Unfortunately, for this direction of the toroidal field, data from the scintillator and foil-based loss detectors are unavailable.

The NUBEAM [34] module of the TRANSP [35] code is instrumental in the analysis. After initial reconstruction of the equilibrium using magnetics and MSE data, spline fits to the thermal plasma profiles as a function of normalized minor radius are obtained; examples appear in figure 3. (Here, the normalized square root of the toroidal flux ρ is employed as flux-surface label.) NUBEAM is run to obtain the fast-ion distribution function and the predicted neutron rate and stored energy are compared with experiment. Often, the calculation overpredicts the measurements. If so, a spatially uniform ad hoc fast-ion diffusion coefficient D_f is implemented in NUBEAM and the results are iterated until agreement between the calculation and the data is obtained. Figure 6 shows an example of a time-dependent ad hoc D_f that produces excellent agreement with the measured neutron rate. Once good agreement is obtained, the EFIT equilibrium reconstruction is repeated using magnetics, MSE, and pressure data.

NUBEAM calculates the fast-ion distribution function F as a function of energy, pitch ($v_\parallel/v$), and (R, z) position. The neutron rate and fast-ion pressure are standard output of the TRANSP code. To obtain predicted FIDA and NPA
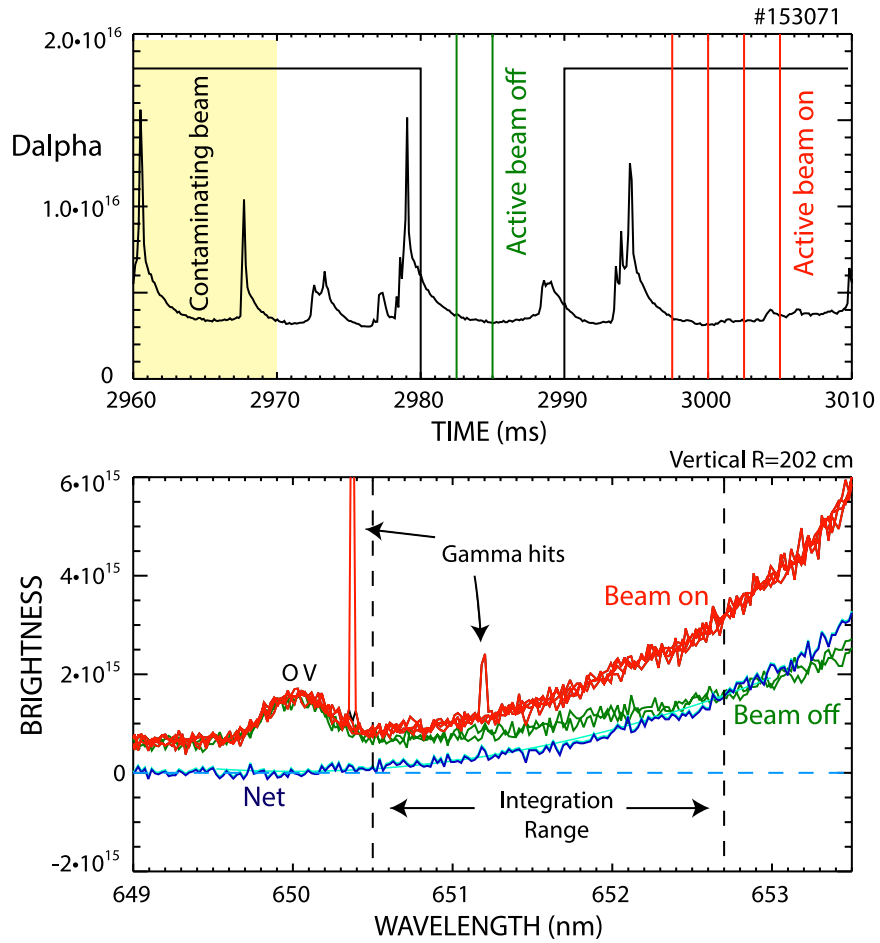
Figure 5. (*a*) Timing diagram. The trace is for a cold D_α monitor of the divertor light. The shaded region indicates a time when a contaminating beam has altered its state. The vertical lines indicate the beginning of accepted time bins for the background and active measurements. (*b*) Vertical FIDA spectra for the time window shown above. When ELMs are properly avoided, all active and all passive time slices overlay. The net signal is the difference between the active and passive signals. The cold oxygen line and elevated signals associated with (n, γ) reactions are also indicated. For the spatial profile, the net signal is integrated between the indicated wavelengths.
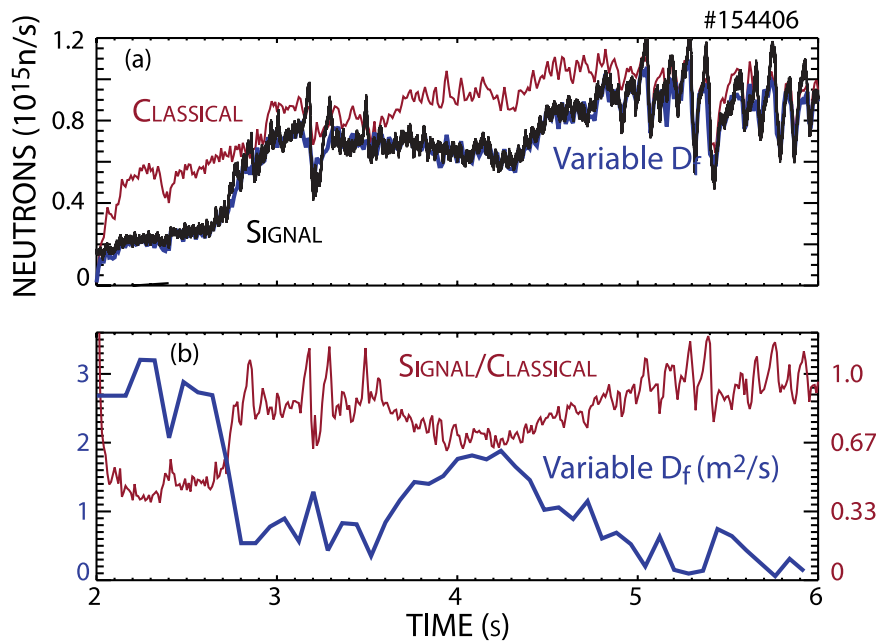
Figure 6. Time evolution of (*a*) the measured and calculated neutron rate and (*b*) the ratio of measured-to-classically predicted neutron rate and the time varying value of D_f used to match the neutron rate in the $q_{min} \simeq 5$ discharge shown in figure 3.

signals, further processing is required. FIDASIM is a synthetic diagnostic code that computes FIDA and NPA signals from an input distribution function F. The original code [36] was written in IDL but the present paper employs the Fortran 90 version developed by Benedikt Geiger [37]. Signals based on NUBEAM calculations without ad hoc diffusion are called 'classical' predictions.

This paper employs two methods to quantify the anomalous fast-ion transport: either compute the ratio of the signal to the classical prediction or find the value of D_f that brings the prediction into agreement with experiment. Figure 6 illustrates the equivalency of these two methods. Between 2.0–2.7 s, the measured neutron rate is approximately half of the classical prediction; alternatively, a huge diffusion coefficient of $D_f \simeq 3\,\mathrm{m^2\,s^{-1}}$ is needed to match experiment. From 2.7–3.5 s, the neutron rate approaches the classical prediction and the required value of D_f is small ($\sim 0.5\,\mathrm{m^2\,s^{-1}}$). As the discharge evolves further, the signal-to-classical ratio decreases at ~ 4 s and D_f increases. Finally, in the latter phase of the discharge, the signal-to-classical ratio is near unity and the required $D_f \rightarrow 0$.

It should be noted that spatially uniform ad hoc diffusion cannot accurately describe the actual wave–particle resonances that cause fast-ion transport. Nevertheless, the use of D_f does provide a convenient quantitative measure of the magnitude of fast-ion transport. The utility and limitations of this model are discussed further in sections 3.1, 4 and 5.

3. Correlation of fast-ion data with AE amplitude

3.1. Comparison of two closely matched discharges

Two cases are selected for detailed comparison: the $q_{min} \gtrsim 1$ and $q_{min} \gtrsim 2$ discharges shown in figure 1. These discharges were acquired sequentially (shot numbers #153071 and #153072, respectively), minimizing the likelihood of changes in diagnostic calibrations that could compromise relative comparisons. They have similar normalized beta, ECCD power, and density. (The $q_{min} \gtrsim 2$ discharge is slightly lower density.) The higher q_{min} discharge has more AE activity (figure 4) and requires more beam power to maintain the same β_N; consequently, the global confinement is poorer in the higher q_{min} shot. Thus, this matched pair of discharges manifests the degraded confinement with increasing q_{min} [8] that motivated this study.

All available diagnostics indicate that the fast-ion confinement is degraded in the higher q_{min} discharge. To quantify the degradation, throughout this section we compare the fast-ion measurements with a set of four NUBEAM calculations of the fast-ion distribution function. The 'classical' pair of calculations have no ad hoc fast-ion diffusion. In the other pair of calculations, a spatially uniform fast-ion diffusion of $D_f = 1.3\,\mathrm{m^2\,s^{-1}}$ is assumed.

Table 1 compares global measures of fast-ion confinement with the NUBEAM calculations. The volume-averaged neutron rate is absolutely calibrated with an uncertainty of $\sim 15\%$ at DIII-D [30] but, in a *relative* comparison of subsequent discharges, changes as small as a few percent are

Table 1. Ratio of measured signal to NUBEAM prediction between 3.2–3.7 s in the $q_{min} \gtrsim 1$ (#153071) and the $q_{min} \gtrsim 2$ (#153072) discharges.

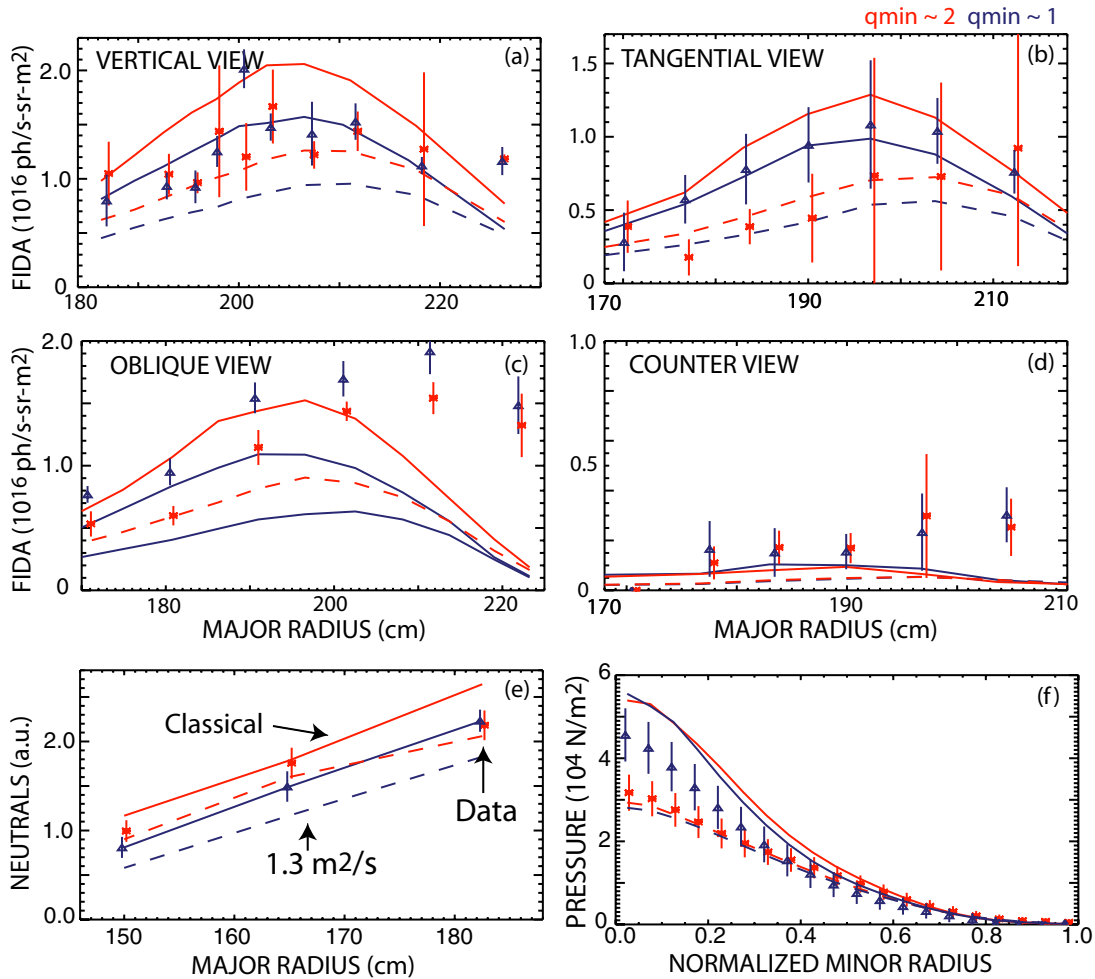|	#153071		#153072	
	Classical	$D_f = 1.3$	Classical	$D_f = 1.3$
Neutrons	89%	124%	61%	91%
W_{fast}	100%	143%	72%	108%

statistically significant. For the $q_{min} \gtrsim 1$ discharge, the ratio of measurement to classical prediction is 89%, which may be consistent with theory. On the other hand, the ratio in the $q_{min} \gtrsim 2$ discharge is clearly discrepant in both absolute magnitude and, especially, relative to discharge #153071. A fast-ion diffusion coefficient of magnitude $D_f \simeq 1.3\,\mathrm{m^2\,s^{-1}}$ is needed to bring the prediction into reasonable agreement with experiment. In contrast, in the low q_{min} discharge, an assumed diffusion coefficient of $D_f \simeq 1.3\,\mathrm{m^2\,s^{-1}}$ results in an underprediction of the neutron rate.

Comparison of the measured fast-ion stored energy W_{fast} with the NUBEAM calculations reinforces these conclusions (table 1). Experimentally, the fast-ion stored energy is inferred from the difference between the equilibrium stored energy and the measured thermal energy. When comparing discharges, use of the EFIT equilibrium that uses exclusively magnetics data minimizes uncertainties associated with the reconstruction procedure. For the low q_{min} discharge, the measured W_{fast} is in good agreement with the classical prediction. In contrast, for the high q_{min} discharge, the measured value is only 72% of the classical prediction. As with the neutrons, assuming $D_f \simeq 1.3\,\mathrm{m^2\,s^{-1}}$ brings the high q_{min} prediction into agreement with experiment but results in an underprediction of W_{fast} in the low q_{min} case.

Figure 7 shows similar comparisons for diagnostics that measure the fast-ion profile. The classically predicted signals are generally higher for the high q_{min} discharge than for the low q_{min} discharge. Experimentally, however, the signals are larger at low q_{min} than at high q_{min} for the oblique and tangential FIDA views (figures 7(*b*, *c*)). As discussed in more detail in section 3.2, these views are most sensitive to the co-passing fast-ion population. For the vertical FIDA views and for the SSNPA measurements, the signals are comparable in the two cases, even though classically the $q_{min} \gtrsim 2$ case should be larger (figures 7(*a*, *e*)). The signals are also comparable for the counter FIDA views (figure 7(*d*)). For the fast-ion pressure profile inferred from the equilibrium reconstruction, nearly equal pressures are predicted classically but the measured pressure is larger at low q_{min} (figure 7(*f*)).

The error bars shown in figure 7 represent random errors inferred from the temporal fluctuations of the signal during the quasi-stationary portion of the discharge. With the exception of the SSNPA data, the figures show absolute comparisons between theory and experiment with no adjustable parameters. The magnitude of possible systematic errors in the FIDA intensity calibration and the FIDASIM calculation are not known precisely but probably are 25% or greater. In contrast, the accuracy of the relative comparison between cases is faithfully represented by the error bars. Thus, the vertical and tangential FIDA views are in good agreement with the

Figure 7. Comparison of classically predicted (solid lines) and predicted signals for $D_f = 1.3 \, \mathrm{m^2 \, s^{-1}}$ (dashed lines) with measurements for the $q_{\min} \gtrsim 2$ discharge #153072 (x) and the $q_{\min} \gtrsim 1$ discharge #153071 (triangle). (*a*) Vertical, (*b*) tangential, (*c*) oblique and (*d*) counter FIDA views. (*e*) SSNPA and (*f*) fast-ion pressure profiles.

classical prediction for the low $q_{\min}$ discharge but disagree with the classical prediction for the high $q_{\min}$ discharge. The FIDA data agree better with the $D_f \simeq 1.3 \, \mathrm{m^2 \, s^{-1}}$ prediction for the high $q_{\min}$ case but large fast-ion diffusion is inconsistent with the data for the low $q_{\min}$ discharge.

The SSNPA diagnostic is not absolutely calibrated so, in figure 7(*e*), the data have been normalized to the classical theoretical prediction in discharge #153071. The relative uncertainties between discharges and channels are accurately represented by the error bars. If one assumes agreement between theory and experiment for the low $q_{\min}$ case, then the high $q_{\min}$ data fit better with the $D_f \simeq 1.3 \, \mathrm{m^2 \, s^{-1}}$ prediction than with the classical prediction.

Systematic uncertainties in the fast-ion pressure profile are difficult to estimate; the relative uncertainties in comparison of the two discharges are probably accurately reflected by the error bars shown in figure 7(*f*). In this case, the data in the low $q_{\min}$ discharge falls between the classical and $D_f \simeq 1.3 \, \mathrm{m^2 \, s^{-1}}$ predictions. The data in the high $q_{\min}$ discharge are in poor agreement with the classical prediction but good agreement with the $D_f \simeq 1.3 \, \mathrm{m^2 \, s^{-1}}$ prediction.

For the counter FIDA views, as a result of the near absence of counter-injection, small signals are both expected

and observed (figure 7(*d*)). The measured signals are larger than predicted for both $q_{\min}$ cases, although some of this discrepancy may be associated with error in the background subtraction for these weak signals with relatively poor signal-to-noise ratios.

To summarize, all fast-ion diagnostics that are sensitive to a populated portion of velocity space show smaller signals than expected in the high $q_{\min}$ discharge. The assumption that $D_f \simeq 1.3 \, \mathrm{m^2 \, s^{-1}}$ gives better agreement with measured signal levels in this discharge. In contrast, in the low $q_{\min}$ discharge, the fast-ion transport is modest ($D_f \lesssim 0.5 \, \mathrm{m^2 \, s^{-1}}$).

The better agreement of the intensities with $D_f \simeq 1.3 \, \mathrm{m^2 \, s^{-1}}$ calculations in the high $q_{\min}$ discharge does not mean that uniform diffusion in all of fast-ion phase space is an accurate model for the transport induced by the AEs. The FIDA data contain additional information. One can compare the shape of the measured spectrum and the shape of the radial profile with theory, independent of amplitude. The fidelity between experiment and theory is quantified by the reduced chi-squared, χ_r^2. For the simulations of the $q_{\min} \gtrsim 2$ discharge, the shape of the vertical FIDA spectra agrees better with the classical simulation that overestimates the intensity than it does with the $D_f = 1.3 \, \mathrm{m^2 \, s^{-1}}$ simulation (table 2). Clearly,

Table 2. Comparison of vertical FIDA data from the nine innermost channels with FIDASIM predictions: ratio of measured-to-predicted brightness, χ_r^2 for the normalized spatial profile, and average χ_r^2 for the normalized spectral shape. Cases with and without fast-ion diffusion in discharges #153071 and #153072 are listed.

Discharge	D_f (m^2/s)	Intensity	Spatial profile	Spectral shape
$q_{min} \gtrsim 1$	0 (classical)	0.96	1.8	1.6
$q_{min} \gtrsim 1$	1.3	1.59	2.2	2.3
$q_{min} \gtrsim 2$	0 (classical)	0.65	0.8	1.1
$q_{min} \gtrsim 2$	1.3	1.09	0.7	1.6
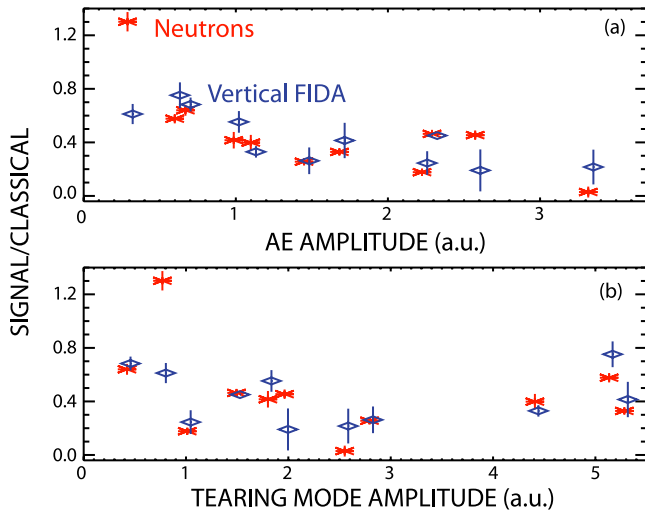
Figure 8. Ratio of measured neutron (x) and vertical FIDA (diamond) signals to classical predictions versus (*a*) AE and (*b*) tearing mode amplitudes. The error bars represent the temporal variation during the stationary portion of the discharge.

although a spatially uniform fast-ion diffusion coefficient is a convenient quantitative measure of the magnitude of the fast-ion transport, it fails to capture the detailed physics of the wave–particle interaction.

3.2. Databases

The trends shown in section 3.1 are generally observed. Degraded fast-ion confinement correlates with enhanced Alfvén activity for all discharges in this study.

Figure 8(*a*) shows the ratio of measured fast-ion signal to classical prediction as a function of AE amplitude for 11 carefully analyzed discharges. The AE amplitude is inferred from the interferometer signals, as discussed in section 2. The correlation is strong for both the neutron signal and the vertical FIDA signal (correlation coefficient $r = -0.74$ and $r = -0.80$, respectively). For the vertical FIDA data, spatial channels between $R = 180$–205 cm are used.

The correlation is much weaker with the amplitude of tearing mode activity (figure 8(*b*)). Here, the tearing mode amplitude is taken from the summed rms amplitude of $n = 1$ and $n = 2$ tearing modes. The correlation of the neutron and vertical-FIDA ratios with tearing mode amplitude is only $r = 0.06$ and $r = 0.00$, respectively. The correlation is also

weak for all other fast-ion signals, such as W_{fast} ($r = -0.16$), oblique FIDA ($r = 0.36$), and tangential FIDA ($r = 0.30$).

Figure 9 shows the correlation of fast-ion signals with AE amplitude for seven fast-ion diagnostics. The figure also shows the velocity-space 'weight function' of each of the measurements. Different fast-ion diagnostics weight different portions of phase space differently; the measured signal is $\int W * F \, d\vec{v} \, d\vec{r}$, where W is the weight function and F is the fast-ion distribution function. For simplicity, the figure just shows the velocity-space dependence of W on the fast-ion energy and pitch $v_\parallel/v$. A typical velocity-space distribution function is shown in figure 9(*h*). In these discharges, the co-passing portion of velocity space ($v_\parallel/v \gtrsim 0.3$) is heavily populated; there are some trapped fast ions ($|v_\parallel/v| \lesssim 0.3$) and very few counter-passing ions ($v_\parallel/v \lesssim -0.3$). All fast-ion diagnostics with strong sensitivity to the heavily populated portion of velocity space show a strong correlation with AE amplitude (figures 9(*a*)–(*d*)). The correlation coefficients for the neutrons, stored energy, oblique FIDA, and vertical FIDA are -0.74, -0.84, -0.67 and -0.80, respectively. The tangential FIDA (figure 9(*e*)) is sensitive to fast ions with higher pitch than the majority of the population; its correlation with AE amplitude is weaker ($r = -0.55$). The SSNPA (figure 9(*f*)) is sensitive to trapped fast ions and the counter FIDA (figure 9(*g*)) is sensitive to counter-passing ions; their signals are weakly correlated with AE amplitude ($r = -0.34$ and -0.28, respectively). The correlations in figure 9 strongly suggests the following underlying causal relationship: AEs degrade the confinement of the co-passing population, so diagnostics that are sensitive to the co-passing population observe reduced signals when the AE amplitude is large.

Detailed NUBEAM and FIDA analysis is labor intensive. The strong correlation between the neutron rate and the AE amplitude (figure 8(*a*)) suggests that a simpler analysis might suffice. TRANSP calculations indicate that beam-plasma reactions dominate in these plasmas. (For example, in discharge #153071, 82% of the reactions are beam plasma, while thermonuclear and beam–beam reactions contribute 9% each.) The expected beam-plasma rate can often be accurately predicted by a zero-dimensional model [38]. To test if a previously developed [30] 0D model can accurately describe the neutron rate in these steady-state scenario discharges, figure 10 a compares the 0D prediction with the NUBEAM calculation for the 11 intensively analyzed discharges discussed above. The agreement is excellent, validating the 0D calculation.

A database has been assembled of 65 quasi-stationary conditions with similar plasma shapes from the 2013 experimental campaign. The conditions span $B_T = 1.0$–2.1 T, $\beta_N = 1.2$–3.6, $\bar{n}_e = 2.4$–3.6 $\times 10^{19}$ m^{-3}, and $q_{min} = 1.1$–2.9. Figure 10(*b*) shows the ratio of measured neutron rate to the 0D prediction versus AE amplitude for these 65 conditions. A strong correlation is observed ($r = -0.66$). In contrast, the correlation with tearing mode amplitude is weak ($r = -0.22$). Surprisingly, in light of the motivation for this study, the correlation with q_{min} is also weak ($r = -0.18$). Stronger correlations with β_N and B_T are observed but that is because those quantities correlate with AE amplitude.
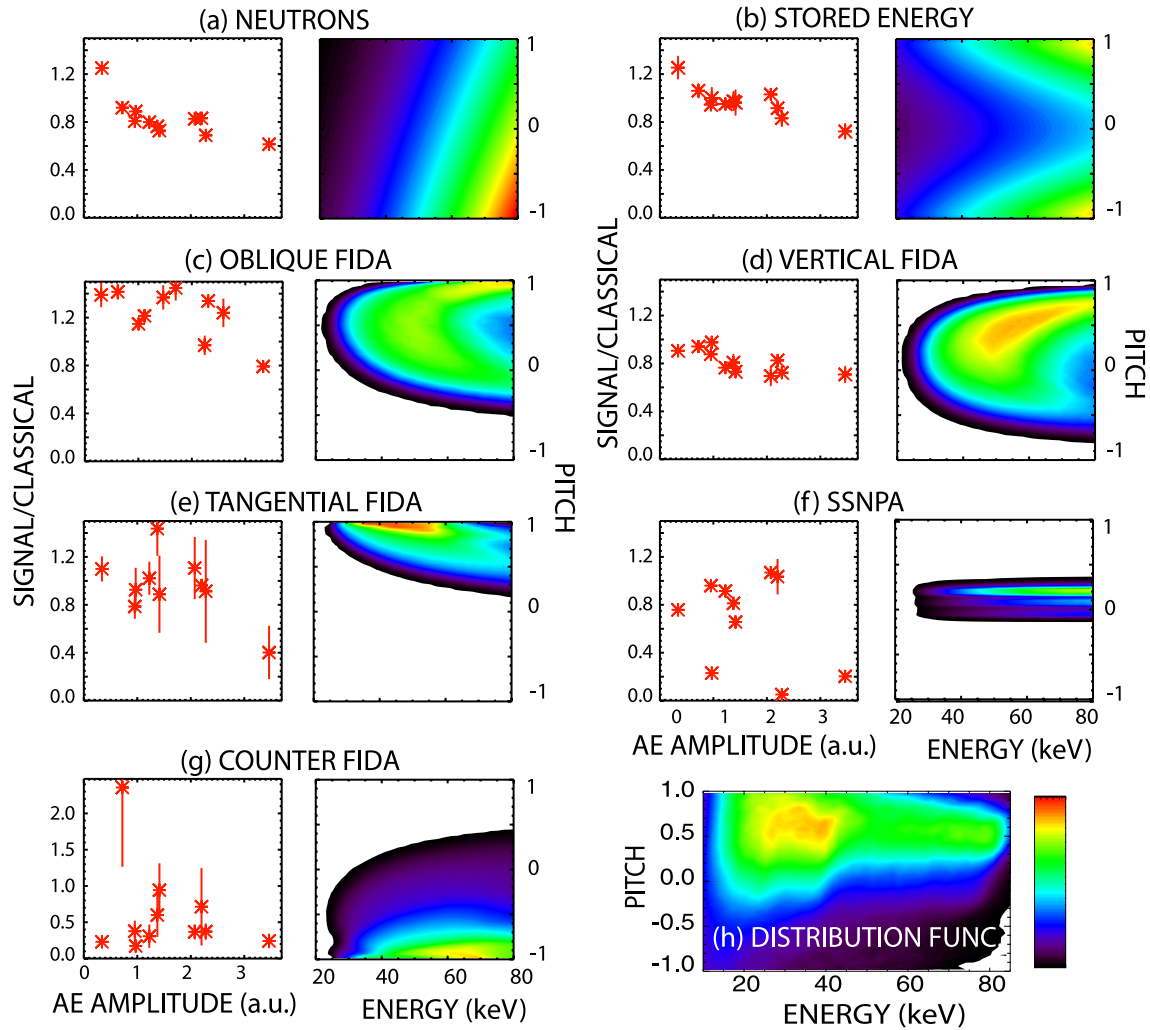
Figure 9. (Left) ratio of measured fast-ion signal to classical prediction versus AE amplitude and (right) velocity-space weight function for seven different fast-ion diagnostics. (*a*) Neutron rate, (*b*) W_{fast}, (*c*) oblique FIDA, (*d*) vertical FIDA, (*e*) Tangential FIDA, (*f*) SSNPA and (*g*) Counter FIDA. (*h*) Classically predicted volume-averaged fast-ion distribution function in discharge #153071. The linear rainbow colour scale used in all eight panels is indicated. The FIDA and SSNPA weight functions are calculated by the Fortran 90 FIDASIM code [37] for discharge #153071 and have been averaged over the same wavelengths and spatial channels as the data. The neutron and W_{fast} weight functions are based on the formulas in the appendix of [49].

3.3. Weak effect of edge modes on fast-ion transport

When the discharge with $q_{min} \simeq 5$ of figure 3 is included on the graph shown in figure 10(*b*), it appears as an outlier. Between 5.4–5.8 s, when the relevant AE activity is weak and the fast-ion confinement is good (signal-to-prediction ratio of 0.94), the calculated AE amplitude is 4.4, i.e. larger than all of the points shown in figure 10(*b*).

This exception highlights a limitation of the interferometer measurement of AE amplitude. There is a very large edge mode in the $q_{min} \simeq 5$ discharge of figure 3. Figure 11 compares a typical AE with the edge mode in the $q_{min} \simeq 5$ discharge. This huge mode, which has an amplitude close to the TAE frequency, dominates the spectrum on the interferometer channels, resulting in a large value of 'AE amplitude'. However, if one examines interior channels, the actual amplitude of central AE activity is relatively weak. Evidently, the Alfvén eigenmodes that degrade fast-ion confinement are in the plasma interior, where most fast ions reside.

4. Global confinement

The conclusion of the previous section is that AEs degrade fast-ion confinement in many steady-state scenario discharges. The issue discussed here is: What are the implications of that degradation for global energy confinement?

The matched pair of discharges discussed in section 3.1 are the basis for the discussion. On average, the $q_{min} \gtrsim 2$ discharge has 18% higher power than the $q_{min} \gtrsim 1$ discharge (figure 1(*c*)) but n_e, T_e and T_i is higher in the low q_{min} discharge. Consequently, the normalized 'H89' global confinement factor is higher in the low q_{min} discharge than in the high q_{min} discharge: 2.2 versus 1.7. Section 3.1 shows that fast-ion signals in the low q_{min} discharge are reasonably well described by classical simulations but the high q_{min} discharge requires fast-ion diffusion of around $1.3\,\mathrm{m^2\,s^{-1}}$ to explain the fast-ion signals. According to TRANSP, in the presence of fast-ion diffusion, the power delivered to the thermal plasma is 39% less than it would be if the fast ions were classical. The diffusion
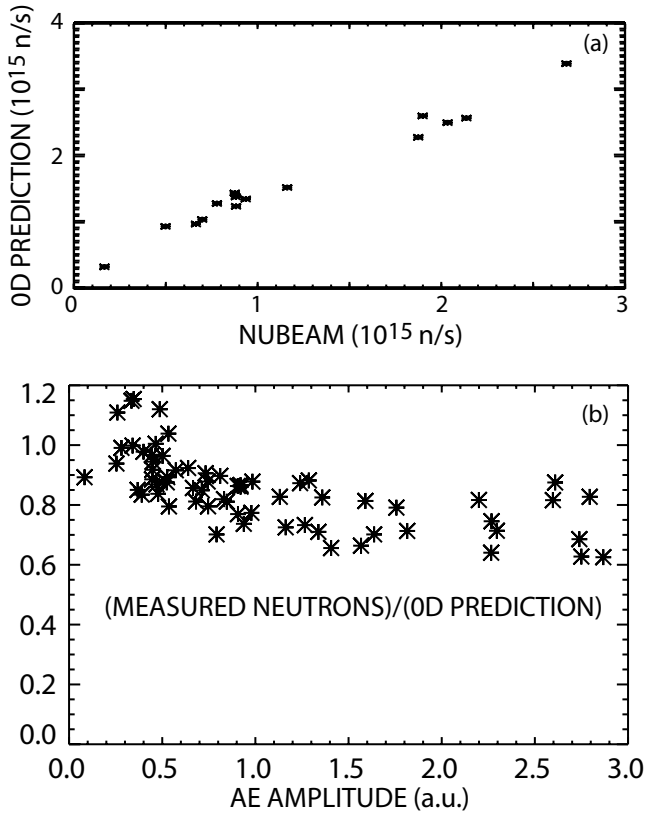
Figure 10. (*a*) Zero-dimensional prediction of the neutron rate [30] versus classical NUBEAM prediction for 11 steady-state discharges. (*b*) Ratio of the measured neutron rate to the zero-dimensional prediction versus AE amplitude for 65 cases.

increases both charge-exchange losses and losses to the walls.

Figure 12 shows the TRANSP power-balance analysis in more detail. Beam heating, ECCD heating, and collisional energy exchange from the ions Q_{ie} are positive inputs to the electron channel, while radiation, convection, and conduction are loss mechanisms. For the thermal ions, beam heating, thermalizing fast ions, and charge exchange from the fast-ion population are positive inputs, while Q_{ie}, convection, and conduction are loss mechanisms. The analysis is shown as a function of ρ for three different cases. For the low q_{min} case under the assumption of classical fast-ion confinement, the electron (ion) conduction power at $\rho = 0.75$ is 2.7 (2.4) MW. The erroneous assumption that the fast ions behave classically in the high q_{min} case implies increased thermal transport (3.0 MW for both ions and electrons). In contrast, the $D_f = 1.3\,\mathrm{m}^2\,\mathrm{s}^{-1}$ simulation implies decreased thermal transport in the high q_{min} case (2.2 and 1.3 MW for the electrons and ions, respectively).

Similarly, analysis in terms of thermal diffusivities implies values of χ_e and χ_i near $5\,\mathrm{m}^2\,\mathrm{s}^{-1}$ at $\rho = 0.75$ in the low q_{min} discharge with classical fast-ion confinement. In the high q_{min} shot, if the fast-ion transport is described by $D_f = 1.3\,\mathrm{m}^2\,\mathrm{s}^{-1}$, χ_e and χ_i are $\sim 26\%$ and $\sim 52\%$ smaller, respectively.

The point of this section is not to argue that thermal confinement is better in the high q_{min} discharges. Spatially uniform ad hoc diffusion is a crude model of fast-ion transport,

so the actual power flow to the thermal channels may differ considerably from the values shown here. The point is that AE-induced fast-ion transport can account for the observed reduction in global confinement at higher q_{min}. Two factors contribute to the reduction. First, since the fast ions classically constitute $\sim 36\%$ of the total, the loss of fast ions directly reduces the stored energy by $\sim 12\%$. Second, the actual power delivered to the thermal plasma is $\sim 39\%$ smaller so, since confinement scales with the square root of the power, the thermal stored energy should be $\sim 18\%$ smaller. These two effects readily account for the observed $\sim 25\%$ reduction in global confinement.

Additional TRANSP simulations test the sensitivity of this conclusion to the assumed ad hoc diffusion model. It is likely that the AE-induced transport acts principally on high-energy, passing particles in the plasma interior. Accordingly, three extreme models of ad hoc diffusion are tested. In one set of simulations, only fast ions with energies above 50 keV suffer diffusion. In another, only fast ions within $\rho \leqslant 0.5$ suffer diffusion. (In reality, AEs are observed out to radii of $\rho \gtrsim 0.7$.) In a third set of simulations, only circulating particles suffer diffusion. In each case, the level of diffusion for the affected particles is adjusted until the predicted neutron rate matches the rate of the spatially uniform simulation with $D_f = 1.3\,\mathrm{m}^2\,\mathrm{s}^{-1}$. Table 3 summarizes the results. As long as the simulations match the neutron rate, irrespective of which portion of fast-ion phase space is affected, the implications for global transport are similar.

5. Conclusions, discussion and outlook

The analysis presented in sections 3 and 4 support the following conclusions.

(1) The strong temporal correlation between AE activity within a shot (figure 6) and strong shot-to-shot correlation between AE amplitude and degraded fast-ion confinement (figures 8(*a*) and 10(*b*)) indicate that AEs cause appreciable fast-ion transport in steady-state scenario DIII-D discharges.

(2) Although tearing modes are a serious impediment to high-performance steady-state operation, their direct impact on fast-ion confinement is weak compared to AEs (figure 8(*b*)).

(3) The co-passing fast-ion population is more strongly affected by AE activity than trapped or counter-passing fast ions (figure 9).

(4) The AE amplitude signal based on interferometer measurements and the ratio of the neutron rate to a zero-dimensional classical prediction provide simple empirical monitors of the AE activity and fast-ion confinement, respectively (figure 10(*b*)).

(5) An ad hoc diffusion model reproduces some features of the fast-ion signals (figure 7 and table 1).

(6) AE-induced fast ion transport accounts for the previously observed degradation in global confinement with increasing q_{min} without any need to invoke degraded thermal confinement (figure 12 and table 3).
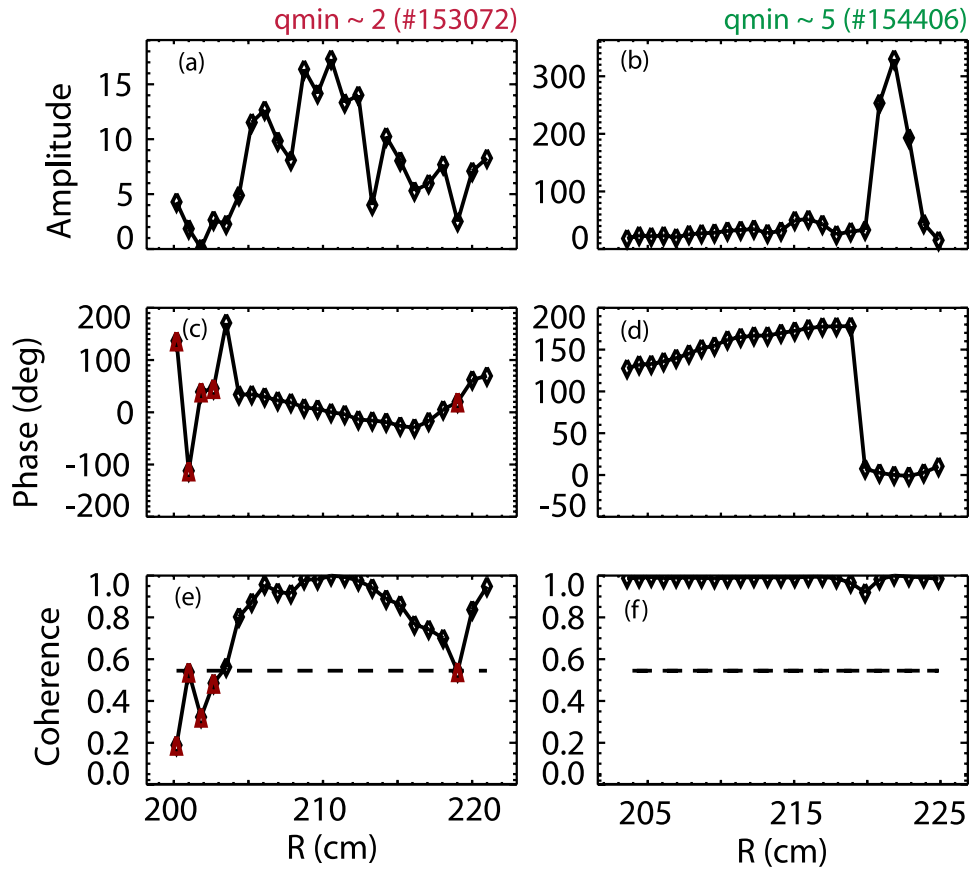
Figure 11. Left: BES measurements of the mode structure for a 94.7 kHz mode at 3.43 s in the $q_{min} \gtrsim 2$ discharge shown in figures 1 and 3. Right: BES measurements of the mode structure for a 54.7 kHz mode at 5.6 s in the $q_{min} \simeq 5$ discharge shown in figures 3 and 6. The mode on the left peaks near $\rho \simeq 0.5$, while the mode on the right is localized outside $\rho = 0.9$.

(7) High q_{min} is *not* intrinsically inimical to good fast-ion confinement; in fact, one of the best discharges has $q_{min} \simeq 5$ (figures 3 and 6).

The first conclusion is hardly surprising. Alfvén eigenmodes in DIII-D cause severe flattening of the fast ion profile during the current ramp [39]. Like the steady-state scenario discharges analyzed here, the spectra in typical current-ramp discharges contain many, small amplitude AEs without appreciable bursting or chirping. Theoretical analysis has shown that the plethora of resonances results in stochastic fast-ion transport [19, 40]. It is extremely likely that the same mechanism operates here.

The second conclusion is also unsurprising. Although tearing modes degrade fast-ion transport above a certain threshold (see, e.g., [41, 42]), very large tearing modes are incompatible with high β_N operation. The discharges selected for this study have relatively modest amplitudes.

The third conclusion is also expected. Co-injected neutral beams create the fast-ion population in this experiment. The fast-ion population is predominately co-passing (figure 9(*h*)). Unstable TAEs are probably driven by co-passing fast ions at the $v_\parallel/v_A = 1/3$ resonance. The resonant particles that drive the instabilities exchange energy with the waves and experience significant change in their constants of motion. It is not surprising that the particles that drive instability suffer the largest transport.

The fourth conclusion is more surprising. The actual resonant interactions that cause fast-ion transport in the experiment occur in narrow regions of velocity and configuration space; moreover, the strength of the interactions differ for different resonances. It is surprising that summing up all of the modes in a broad frequency band yields an 'AE amplitude' that correlates well with fast-ion measurements. Similarly, it is surprising that a quantity like the volume-averaged neutron rate that integrates over all of phase space without regard to the details of the resonant interaction correlates so strongly with this 'AE amplitude.' Presumably, the explanation for this success is due to the nature of fast-ion transport in this regime. A previous study of Alfvén eigenmodes during the current ramp [13] found that the summed amplitude of AEs as measured by ECE correlated well with changes in the calculated linear stability. Another finding of that work was that, owing to the many small-amplitude resonances that span much of phase space, the fast-ion transport was 'stiff' and tended to relax toward a critical gradient. If similar physics is operative here (as suggested by the similar spectra), the many modes ultimately interact with most of the fast ions, causing averaged quantities to be representative of the bulk fast-ion population.

In light of the complexity of the true interaction, the fifth conclusion is also rather surprising. Clearly, a spatially
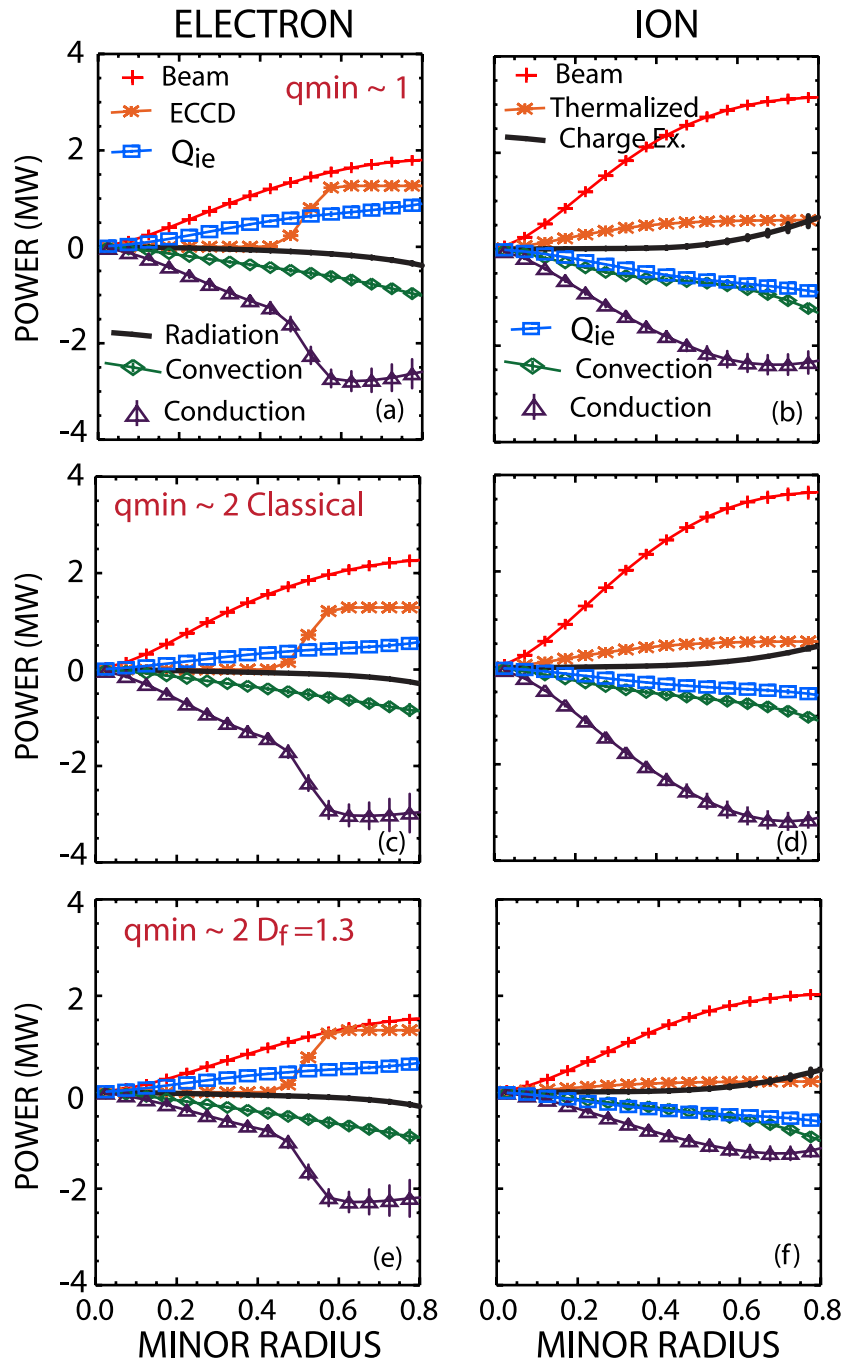
Figure 12. TRANSP electron (*a*),(*c*),(*e*) and ion (*b*),(*d*),(*f*) power-balance calculations for three different cases. (*a*),(*b*) The $q_{min} \gtrsim 1$ (#153071) discharge with classical fast ions. (*c*),(*d*) The $q_{min} \gtrsim 2$ (#153072) discharge with classical fast ions. (*e*),(*f*) the $q_{min} \gtrsim 2$ discharge with $D_f = 1.3 \, \text{m}^2 \, \text{s}^{-1}$. The power flows are integrated over volume up to the integrated minor radius ρ. The electron terms represent beam power to the electrons (+), ECCD power (*), collisional heating by the ions (square), radiation (solid line), convection (diamond), and conduction (triangle). The ion terms represent beam power to the ions (+), thermalized fast ions transferred to the thermal ion population (*), net charge exchange (solid line), collisional losses to the electrons (square), convection (diamond) and conduction (triangle).

uniform D_f that operates on all velocities cannot describe the actual wave–particle interaction. Nevertheless, if many waves ultimately interact with most fast ions, this coarse empirical approach could be surprisingly robust. To some extent, this justifies the analysis in previous papers such as [6, 16]. The main effect of the AEs seems to be to reduce the amplitude of all fast-ion signals, as shown in figure 7. It should be noted, however, that a constant D_f does not provide

the best fit to all features of the experimental data (table 2). Presumably, an improved model of the fast-ion transport would accurately reproduce the spectral and radial shapes, as well as the intensity.

The sixth and seventh conclusions have important practical implications. Some scaling arguments indicate that high q_{min} could be a favorable regime for a steady-state tokamak [1]. If the thermal confinement is not degraded at high

Table 3. Percent reduction in calculated fast-ion stored energy, electron conduction losses, and ion conduction losses relative to the classical prediction for four different models of fast-ion transport.

Model	D_f (m²/s)	Fast ions	Elec. Cond.	Cond. Ion
All fast ions	1.3	35	26	56
Above 50 keV	1.4	34	25	48
$\rho \leqslant 0.5$	1.4	35	26	56
Only passing	2.8	35	25	57

q_{min} then, if regimes with weak AE activity exist, attractive steady-state operation could be accessible.

This paper represents the first stage of a two-part project. The goal of the first stage is to understand empirically fast-ion confinement and its effect upon global confinement in steady-state scenario DIII-D discharges. Now that it has been established that Alfvén eigenmode transport is an important effect, the second stage is to understand the physics of the induced transport in this regime. To that end, theoretical analysis similar to that found in [13] is envisioned. Linear AE stability will be analyzed with the ideal MHD code NOVA-K [43], the gyrofluid code TAEFL [44], and the gyrokinetic code GYRO [45]. Hopefully, this will explain why the $q_{min} \simeq 5$ discharge with an ITB has weaker AE activity than other high q_{min} discharges. We also intend to test if critical gradient models based upon NOVA-K [46] and GYRO [47] can describe the observed fast-ion profiles. Another line of research is to incorporate a physics-based fast-ion transport model into NUBEAM [48]. Finally, if one or more of these approaches is successful, we will use AE theory to predict attractive operational scenarios and investigate them experimentally.

Acknowledgments

References

[1] Luce T C 2011 *Phys. Plasma* **18** 030501
[2] Gormezano C *et al* 2007 *Nucl. Fusion* **47** S285
[3] Petty C C *et al* 2000 *Plasma Phys. Control. Fusion* **42** B75
[4] Strait E J *et al* 1995 *Phys. Rev. Lett.* **75** 4421
[5] Ferron J R *et al* 2011 *Nucl. Fusion* **51** 063026
[6] Holcomb C T *et al* 2012 *Phys. Plasma* **19** 032501
[7] Turco F *et al* 2012 *Phys. Plasma* **19** 122506
[8] Ferron J R *et al* 2013 *Phys. Plasma* **20** 092504
[9] Yushmanov P N *et al* 1990 *Nucl. Fusion* **30** 1999
[10] Wong K-L 1999 *Plasma Phys. Control. Fusion* **41** R1
[11] Fasoli A *et al* 2007 *Nucl. Fusion* **47** S264
[12] Heidbrink W W 2008 *Phys. Plasma* **15** 055501
[13] Heidbrink W W *et al* 2013 *Nucl. Fusion* **53** 093006
[14] Wong K L *et al* 2004 *Phys. Rev. Lett.* **93** 085002
[15] Wong K L *et al* 2005 *Nucl. Fusion* **45** 30
[16] Murakami M *et al* 2006 *Phys. Plasma* **13** 056106
[17] Ide S *et al* 2005 *Nucl. Fusion* **45** S48
[18] Ishikawa M *et al* 2006 *Nucl. Fusion* **46** S898
[19] White R B, Gorelenkov N, Heidbrink W W and Vanzeeland M A 2010 *Plasma Phys. Control. Fusion* **52** 045012
[20] Holcomb C T *et al* 2009 *Phys. Plasma* **16** 056116
[21] Murakami M *et al* 2009 *Nucl. Fusion* **49** 065031
[22] Carlstrom T N *et al* 1992 *Rev. Sci. Instrum.* **63** 4901
[23] Carlstrom T N, Ahlgren D R and Crosbie J 1988 *Rev. Sci. Instrum.* **59** 1063
[24] Gohil P, Burrell K H, Groebner R J and Seraydarian R P 1990 *Rev. Sci. Instrum.* **61** 2949
[25] Lao L L, St John H, Stambaugh R D, Kellman A G and Pfeiffer W 1985 *Nucl. Fusion* **25** 1611
[26] Rice B W, Nilson D G and Wroblewski D 1995 *Rev. Sci. Instrum.* **66** 373
[27] Van Zeeland M A *et al* 2005 *Plasma Phys. Control. Fusion* **47** L31
[28] Strait E J 2006 *Rev. Sci. Instrum.* **77** 023502
[29] Gupta D K, Fonck R J, Mckee G R, Schlossberg D J and Shafer M W 2004 *Rev. Sci. Instrum.* **75** 3493
[30] Heidbrink W W, Taylor P L and Phillips J A 1997 *Rev. Sci. Instrum.* **68** 536
[31] Muscatello C M, Heidbrink W W, Taussig D and Burrell K H 2010 *Rev. Sci. Instrum.* **81** 10D316
[32] Grierson B A *et al* 2012 *Rev. Sci. Instrum.* **83** 10D529
[33] Zhu Y B, Bortolon A, Heidbrink W W, Celle S L and Roquemore A L 2012 *Rev. Sci. Instrum.* **83** 10D304
[34] Pankin A, Mccune D, Andre R, Bateman G and Kritz A 2004 *Comput. Phys. Commun.* **159** 157
[35] Budny R V 1994 *Nucl. Fusion* **34** 1247, and references therein
[36] Heidbrink W W, Liu D, Luo Y, Ruskov E and Geiger B 2011 *Commun. Comput. Phys.* **10** 716
[37] Geiger B 2013 Fast-ion transport studies using FIDA spectroscopy at the ASDEX Upgrade tokamak *PhD Thesis* Ludwig-Maximilians-Universität München
[38] Strachan J D *et al* 1981 *Nucl. Fusion* **21** 67
[39] Heidbrink W W *et al* 2007 *Phys. Rev. Lett.* **99** 245002
[40] White R B, Gorelenkov N, Heidbrink W W and Vanzeeland M A 2010 *Phys. Plasma* **17** 056107
[41] Carolipio E M, Heidbrink W W, Forest C B and White R B 2002 *Nucl. Fusion* **42** 853
[42] García-Muñoz M *et al* 2007 *Nucl. Fusion* **47** L10
[43] Gorelenkov N N, Cheng C Z and Fu G 1999 *Phys. Plasma* **6** 2802
[44] Spong D A 2013 *Nucl. Fusion* **53** 053008
[45] Bass E M and Waltz R E 2010 *Phys. Plasma* **17** 112319
[46] Ghantous K, Gorelenkov N N, Berk H L, Heidbrink W W and Van Zeeland M A 2012 *Phys. Plasma* **19** 092511
[47] Waltz R E and Bass E M 2014 *Nucl. Fusion* **54** at press
[48] Podestà M, Gorelenkova M and White R B 2014 *Plasma Phys. Control. Fusion* **56** 055003
[49] Heidbrink W W *et al* 2007 *Plasma Phys. Control. Fusion* **49** 1457